

Structural, Magnetic, Dielectric and Energy Storage Analysis of $\text{CoFe}_2\text{O}_4@ \text{BaTiO}_3$ and $\text{BaTiO}_3@ \text{CoFe}_2\text{O}_4$ Core-Shell Nano- Composites

NIDHI SHEORAN

Deenbandhu Chhotu Ram University of Science and Technology

Vinod Kumar (✉ vinod.phy@dcrustm.org)

Deenbandhu Chhotu Ram University of Science and Technology

Ashok Kumar

Deenbandhu Chhotu Ram University of Science and Technology

Research Article

Keywords: Nanocomposites, Ferroelectric, Ferromagnetic, Core-shell

Posted Date: June 8th, 2020

DOI: <https://doi.org/10.21203/rs.3.rs-33291/v1>

License:   This work is licensed under a Creative Commons Attribution 4.0 International License.

[Read Full License](#)

Abstract

Nano size spinel ferrite CoFe_2O_4 (CFO), ferroelectric BaTiO_3 (BTO) and their core-shell nanocomposites BTO@CFO and CFO@BTO were synthesized using combination of chemical co-precipitation and sol-gel route respectively. The phase formation and crystallinity of bare CFO, BTO and their core-shell nanocomposites were verified via X-ray diffraction pattern (XRD). High resolution transmission electron microscopy (HRTEM) revealed the core-shell structure of the nanocomposites. Magnetization measurements exhibit ferromagnetic behaviour of all the samples except BTO in which superposition of weak ferromagnetic and diamagnetic response occurred due to its nanostructure. Magnetization versus temperature (M-T plot) measurements show anomaly near ferroelectric to paraelectric phase transition of BTO. Also, dielectric constant (ϵ') and tangent loss ($\tan\delta$) variation with respect to frequency (10^2 to 10^6 Hz) and temperature (300-700 K) were presented. ϵ' -T curve of nanocomposites exhibit anomaly at the same temperature as observed in M-T plot of nanocomposites that indicate the inherent magneto-electric coupling in nanocomposites. Energy storage properties of BTO and nanocomposites have been examined via P-E loop analysis and confirmed that the sample CFO@BTO exhibit maximum energy storage efficiency.

1 Introduction

Multiferroic materials perform important role in development of multifunctional devices that simultaneously show ferroelectric, ferromagnetic, and piezo-elastic orders in the same phase [1–2]. Materials revealing spontaneous magnetization due to spontaneous polarization by a large coupling interaction could permit the capability to control electric field using an magnetic field, and vice versa [3]. This is the consequence of magnetoelectric phenomenon. Scientific communities paying attention on these multiferroic materials because of its possible applications in several multifunction devices, like memory elements with multiple states, transducers, spintronics, sensors and terahertz radiation [1, 4]. As a result of mutual exclusivity of ferroelectricity and ferromagnetic arrangement, the existence of single-phase multiferroic materials like BiFeO_3 , BiMnO_3 , and YMnO_3 , are very small [1]. Additionally, the magnetic response, dielectric constant and magnetic permeability of single-phase multiferroics are restricted in accordance with phenomenological theory [5]. Therefore, to produce single-phase multiferroic compounds having high magnetoelectric coupling to use it as multifunction devices is hard [6]. In the last two decades, most of the work have been accomplished to remove the drawbacks of single-phase multiferroic materials. Earlier studies show that composite of multiphase multiferroics possesses high magnetoelectric coupling (ME) coefficients having large values of magnetization and polarization than single phase multiferroic materials [7–9]. ME coupling in composites occurs at the boundary of magnetic and ferroelectric phases. Nanocomposites propose an interesting and effective technique for novelty in functioning materials. However, the synthesis mechanism of nanocomposites has a number of disadvantages, like differences in thermal expansion, grain boundaries, and discrepancies in between crystal parameters. Thus to buried these problems, core-shell nanostructures consisting of core as ferromagnetic materials and shell as ferroelectric materials or vice versa, are excellent candidates. Core-

shell nanocomposite provide modified properties which rises either from the core or the shell or the joint effect of core and shell which make it highly functional materials [10]. Although, various research have been reported on the core/shell type nanostructures $\text{CoFe}_2\text{O}_4/\text{BaTiO}_3$, $\text{CoFe}_2\text{O}_4/\text{BiFeO}_3$ and $\text{NiFe}_2\text{O}_4/\text{BiFeO}_3$ [11–13], but still there have been a lack of systematic reports on development of uniform core/shell nanostructures of multiferroic materials. Core-shell nanocomposite having very strong interactions are anticipated to be (a) a medium that transfer strain ideally, (b) Dielectric layer as a shell reduces the leakage problem by decrease the conductivity of the composites and (c) Enhancement in magnetoelectric coupling [14–15]. $\text{BaTiO}_3/\text{CoFe}_2\text{O}_4$ composites possess better magnetoelectric properties as a result of individual phases contribution. Perovskite BaTiO_3 (BTO) is an excellent efficient ceramic having interesting ferroelectric properties, and its optical properties, such as multilayer ceramic capacitors (MLCC), converters, actuators, random access ferroelectric memory devices with energy storage applications [16]. BaTiO_3 mainly exhibit ferroelectric property but it can be multiferroic if it synthesized at nanoscale. So in present work we explore multiferroic properties of BaTiO_3 by synthesizing it via sol gel method to develop nanoparticles of BaTiO_3 . Spinel ferrite CoFe_2O_4 (CFO) possesses outstanding electrical, magnetic and optical properties, especially on a nanometre scale. Thus we explore the multifunctional properties of CFO@BTO and BTO@CFO core-shell nanocomposite by study their structural, magnetic, dielectric and energy storage properties.

2 Experimental

2.1 Synthesis of BTO nanoparticles and CFO@BTO nanocomposite

BTO nanoparticles were synthesized via sol-gel technique. Firstly barium carbonate (1.9 gm) was dissolved in 10 ml ethanol with continuous stirring for half an hour at room temperature. In parallel, titanium tetra isopropoxide (2.8 ml) was dissolved in 10 ml ethanol with continuous heating (at 80 °C) and stirring on hot plate separately for half an hour. Later, these two solutions were mixed in a single beaker with continuous stirring for 20 minute. After that citric acid (4.20 gm) was added in the mixed solution followed by continuous stirring and heating at 80 °C for half an hour. Finally, a thick white paste was formed in form of gel. Further, this gel was dried inside the oven at 120 °C for two hour and then it was annealed at 600 °C and 800 °C for 2 hour in programmable muffle furnace to get barium titanate powder. This powder was crushed in mortar pestle to get fine nanoparticles of BTO.

Further, CFO@ BTO nanocomposite of 1:1 weight ratio of CFO and BTO were synthesized by following the same synthesis steps of BTO except one additional step in which already synthesized CFO nanoparticles were added near the step of gel formation. The synthesis steps of CFO nanoparticles are given in Sect. 2.2. Finally, the obtained nanocomposites were annealed at 800 °C.

2.2 Synthesis of CFO and BTO@CFO nanocomposite

CFO nanoparticles were prepared by chemical co-precipitation method. Cobalt nitrate $\text{Co}(\text{NO}_3)_2 \cdot 6\text{H}_2\text{O}$ (6.39 gm) and iron nitrate $\text{Fe}(\text{NO}_3)_3 \cdot 9\text{H}_2\text{O}$ (17.57 gm) were dissolved in 60 ml of distilled water and stirring have to be done for 30 minute to get the homogeneous solution. Oleic acid as a surfactant (10 ml) was added to prevent the agglomeration of the particles, followed by stirring for about 30 minute at 80 °C. After that the precipitating agent liquid NH_3 was added drop-wise under constant stirring so as to attain the pH of solution equal to 9. The precipitate was then finally dried at 100 °C on hot plate and crushed by an agate mortar to get nanoparticles. Further, the produced CFO nanoparticles were annealed at 800 °C for 2 hour.

The synthesis steps of BTO@CFO nanocomposite of 1:1 weight ratio of BTO and CFO are same as of synthesis steps of CFO nanoparticles except one additional step of addition of BTO nanoparticles before precipitation step. Finally, the obtained nanocomposites were annealed at 800 °C.

2.3 Instrumentation Specifications

Rigaku Ultima IV powder X-ray diffractometer with $\text{CuK}\alpha$ radiation was used for structural and phase analysis of developed samples. HRTEM (Tecnai G^2 20, S-Twin (FEI)) employ the identification of core-shell nanostructures. Vibrating sample magnetometer (Lakeshore Model 7410) of magnetic field range ± 2 T was used for room temperature and temperature dependent magnetisation measurements. For temperature dependent measurements constant magnetic field of 500 gauss and temperature range 300 to 800 K were used. Impedance analyser having frequency range 100 Hz to 1 MHz (Wayne Kerr-6500B) was used for dielectric measurements. Ferroelectric measurements were carried out by using P–E Loop Tracer (Marine India) at room temperature.

3 Results And Discussion

3.1 XRD analysis

X-ray diffraction pattern of synthesized BTO at different annealing temperature are shown in figure1. BTO1 represent the raw sample without annealing and BTO2, BTO3 represent the samples annealed at 600 and 800 °C temperature of BTO powder. The XRD results shows that BTO1 have very small crystallinity and phases do not grow at this temperature and at annealing temperature 600 °C the BTO phases appeared with some extra peak of residue material BaCO_3 . The causes of presence of residue BaCO_3 peaks is the incomplete reaction between the precursors to form BTO.

These BaCO_3 phases of orthorhombic structure are identified by ICSD file number 91888. Finally the pure phase of BTO having fine crystallinity was obtained after annealing at temperature 800 °C. At this temperature the intensity of BTO phase is enhanced and all the extra peaks of residue material BaCO_3 disappeared. The peaks of perovskite BTO phase with tetragonal structure are identified as ICSD file number 29148.

Figure 2 represents XRD pattern of bare CFO, BTO and their Core-Shell nanocomposites CFO@BTO and BTO@CFO. XRD pattern of both the core shell nanocomposites revealed characteristics peaks of ferrite (CFO) and ferroelectric (BTO) phases. All peaks of nanocomposites are indexed as shown in figure 2, which is analogous to the peak location and intensities recorded in ICSD data file for CFO and BTO phase. Also, no any other undesired extra impurity phases are detected in the XRD pattern that indicate in between these two phases chemical reaction is absent.

The lattice parameter for CFO are measured by the equation

$$a = d\sqrt{h^2 + k^2 + l^2} \quad (6.1)$$

where h, k, l denotes miller indices to equivalent planes. For BTO, lattice parameters a and c are measured by equation

$$\frac{1}{d^2} = \frac{h^2 + k^2}{a^2} + \frac{l^2}{c^2} \quad (6.2)$$

The calculated values of lattice parameters of BTO and CFO phases are tabulated in table 1. These lattice parameters are nearly matched with the earlier results [17-18]. Further, average crystallite size (D) was calculated by the Debye-Scherrer equation,

$$D = \frac{k\lambda}{\beta \cos\theta} \quad (6.3)$$

(where, k is symbol for shape factor with 0.89 value, λ represent wavelength of X-rays, peak position determined by θ and β stands for full width at half maxima for maximum intense peak).

Table 1
Lattice Parameters and crystallite size of CFO, BTO@CFO,
CFO@BTO and BTO nanoparticles

Sample	Lattice parameters			Crystallite size	
	(Å)			D (nm)	
	CFO	BTO		CFO	BTO
	a	a = b	c		
CFO	8.382	-	-	29	-
BTO@CFO	8.349	3.993	3.991	32	38
CFO@BTO	8.333	3.995	3.998	34	37
BTO	-	3.999	4.010	-	39

3.2 Microscopic analysis

The HRTEM micrograph of BTO nanoparticles and CFO@BTO nanocomposite are shown in figure 3(a) and (b) respectively. The magnified view of CFO@BTO nanocomposite are depicted in figure 3 (c). Figure 3(a) clearly shows tetragonal BTO nanoparticles with particle size ~ 49 nm which is accordance with the XRD results. Figure 3(b) & (c) represent clearly the formation of core (dark) -shell (bright) nanostructures of CFO@BTO nanocomposite as a result of difference in transmission intensities of BTO and CFO phases. The core identified as CFO and shell as BTO because of measured value of lattice spacing $d = 0.251$ nm in dark region which is corresponding to CFO phase and $d = 0.283$ nm in bright region that correspond to BTO phase. Further, from figure 3 (b) the measured value of core diameter is ~ 50 nm and having shell thickness ~ 17.5 nm. Magnetic CFO nanoparticles form agglomerates in BTO matrix.

Figure 4(a) shows HRTEM micrograph of BTO @CFO nanocomposite with the presence of some agglomerates and arbitrary mixture of BTO and CFO phases. Figure 4 (b) shows the magnified view of this nanocomposite that revealed the interplanar distances $d = 0.252$ nm in bright part and $d = 0.282$ nm in dark part which corresponds to the BTO and CFO phases respectively. In figure 4 (a) the magnetic CFO nanoparticles form agglomerates around the BTO core therefore it is difficult to measure thickness of shell and core. However, average particle size of BTO@CFO nanocomposite is 56 nm

3.3 Magnetic analysis

M-H curve of BTO nanoparticles exhibit superposition of diamagnetic and weak ferromagnetic contributions as revealed by figure 5 (a). Change in magnetization M in the vicinity of $\pm H_c$ ($H_c \sim 830$ gauss is coercive field strength) represent weak ferromagnetic behaviour. The M-H plot without

diamagnetic contribution is shown figure5 (b). The observed value of spontaneous magnetization (0.003) is analogous to the previous reported results [19]. Such type of behaviour in BTO nanoparticles is attributed to presence of defects as oxygen vacancies on the grains surfaces. These oxygen vacancies at surface generate couple of Ti^{3+} - O in the interstitial position and Ti^{3+} - V_o at the surface where, V_o is void due to oxygen deficiency[20]. These couples ferromagnetically interact as shown by mechanism in figure 6. Thus weak ferromagnetism arises in BTO nanoparticles due to its surface defects.

In figure7 the M-H loop of CFO, CFO@BTO and BTO@CFO exhibit hysteresis and show ferromagnetic behaviour. The saturation magnetization (M_s), remnant magnetization (M_r), coercivity (H_c), anisotropy constant (K) and squareness ratio (S) values are tabulated in table2. Both the nanocomposites exhibit reduced value of magnetizations than CFO nanoparticles. The magnetic moments in the nanocomposites arises mostly due to CFO nanoparticles, as BTO exhibit very little magnetization. CFO@BTO having slightly high value of magnetization than BTO@CFO. As in core-shell composites the core and shell material preserve their properties individually therefore magnetic core CFO exhibit large magnetization. Two type of magnetic interaction are occurred in the composites samples. One is super-exchange interaction within CFO nanoparticles and another is exchange interaction at interface of BTO and CFO phases. Thus thin layer of 17.5 nm of BTO in CFO@BTO sample favored the magnetization due to surface exchange interaction at the interface [21-22]. However, surface spin canting occur due to thin layer of CFO nanoparticles in BTO@CFO nanocomposite that reduced magnetization.

To establish the domain structure of the CFO phase and composites the squareness ratio (S) were estimated as shown in table2. The observed values of S indicates that both CFO phase and nanocomposites are multidomain structured ($S < 0.5$). To investigate the magnetic transition temperature (T_c) of CFO, CFO@BTO and BTO@CFO nanoparticles, M-T plot having applied magnetic field of 500 gauss are revealed in figure8(a), (b)&(c) respectively. Figure8(a) shows that at low temperature there is small variation in magnetization and drastic variation occur at high temperature. This sharp decrease in magnetization at high temperature can be withdrawal of ferrimagnetic behavior at magnetic transition temperature T_c (= 734K) for pure CFO nanoparticles. Figure8 (b) and (c) shows this magnetic transition temperature at T_c (= 653K) and T_c (= 610K) for CFO@BTO and BTO@CFO nanocomposites respectively. It has been considered that the magnetic moment decreases with increasing temperature, causing a phase transition from ferrimagnetism to paramagnetism. This is due to increased thermal randomization of the magnetic moment at enhancing temperature [23].

Table 2
Saturation magnetization (M_s), remanence magnetization (M_r) coercivity (H_c), S (squareness ratio), T_c (Curie temperature) of CFO, CFO@BTO and BTO@CFO nanoparticles.

Samples	M_s (emu/g)	M_r (emu/g)	H_c (gauss)	$S = M_r / M_s$	T_c (K)	
					BTO	CFO
CFO	62.25	26.72	1687	0.43	-	734
CFO@BTO	32.61	13.74	1402	0.42	362	653
BTO@CFO	31.33	14.04	1351	0.44	349	610

Lyubutin et al. [24] investigated the antiferromagnetic arrangement of CFO at low-temperature (non-collinear order of the magnetic moments of Fe and Co) and recognized a canted magnetic structure. When heating is applied with an applied magnetic field, magnetic arrangement in CFO nanoparticles is constantly transformed from an canted state to a collinear one, which leads to an increase in magnetization. However, it has been shown that T_c values in nanocomposites are slightly reduced compared to pure CFO. This decrement in the T_c values for the nanocomposites are due to the diffusion of BTO domain into the spinel lattice that weaken the super exchange interaction [25]. This weakening of super exchange interaction is the result of increase in the separation of magnetic moments at A and B position of the spinel structure. Weak super-exchange interactions are more effected by the thermal motion, that results in reduction of T_c of nanocomposites. In figure 8(b) and (c) M-T measurements shows the magnetic anomaly at 362 K and 349 K respectively. These magnetic anomaly in both the nanocomposite exhibit the ferroelectric phase transition of BTO because these anomalies lies near the standard ferroelectric $T_c \sim 390$ K of BTO. Also, increase in magnetization near T_c of BTO in both the nanocomposites might be due to sharp increase in compressive strain [26]. Thus these anomaly indicate the magnetoelectric coupling effect in both the nanocomposites.

3.4 Dielectric analysis

Figure 9 (a) depicted change in dielectric constant (ϵ') and 9(b) tangent loss ($\tan\delta$) with respect to frequency range 10^2 to 10^6 Hz for all the samples. The dielectric constant of all samples exhibit strong dependence on frequency, having larger value at low frequencies and decreases on growing frequency and attained the continual behaviour like a typical dielectrics. Largest dielectric constant value at small frequency region may be demonstrated on ground of polarization of charge by virtue of non-homogeneous dielectric structure and Maxwell-Wagner space charge polarization, that accordant to Koops phenomenological theory. These models play major role in such type of multiphase composites [27-31]. In this model, the dielectric structure of ferrite and composites were supposed to be consist of

good conducting layers of grain surrounded by weakly conducting grain boundaries. At small frequencies more polarization occur due to the active participation of grain boundary and fast response of it to the applied field. Therefore, more charge accumulation take place at the grain boundary interface which result in high dielectric constant. In small frequency region, electric dipole is in phase with the applied field frequency but in large frequency region these dipoles unable to pursue the fast changing in applied field. Thus CFO@BTO exhibit high value of dielectric constant than BTO@CFO due to its core-shell structure in which there is ordered arrangement of ferroelectric and ferrite layer. But in BTO@CFO due to agglomeration of CFO nanoparticles around BTO core large conducting channel formation take place that decrease the value of dielectric constant. The $\tan\delta$ represent the tangent loss in the sample which measure the electrical energy loss due to applied electric field at various frequencies. The nanocomposites exhibit small value of tangent loss than BTO and CFO phase. Therefore these nanocomposites are useful for high frequency microwave devices.

Figure 10 displays change in dielectric constant with respect to temperature of nanocomposites and BTO (in inset) at frequency 10 kHz. The dielectric constant increases upto first transition temperature of range 350 to 370 K then it reaches to a second maximum and then decrease again. The increment in dielectric constant with temperature are ascribed to interfacial polarization at ferrite / ferroelectric boundary and also due to the mechanism of hopping conduction, which is a process of thermal activation [28]. The first anomaly in the temperature range 350-370 K correspond to ferroelectric phase transition of BTO phase which suggest presence ferroelectric phase in these nanocomposites. The another peak in the temperature range 640-680 K attributed to the transition in dielectric constant close to T_c of CFO phase [8].

Near transition temperature, large dielectric constant are attributed to effect of temperature alteration on domain wall motion. At lower temperature the domain wall contributed to small dielectric constant because of difficulties in movement of domains [32]. However, at transition temperature the high dielectric constant value is attributed to domain wall motion and beyond the transition temperature, it decreases due to difficulty in the orientation of domains in path of functional electric field [33]. The curie temperature of BTO is ~ 390 K. But here we observed decrease in curie temperature (T_c) for both BTO nanoparticles and nanocomposites which can be ascribed to the intrinsic size effect. As due to nanosized (< 100 nm) BTO induces stress inside the grain, thereby inhibiting the movement of domain wall. Thus the competition between the shrinkage of surface bonds and the pinning of domain walls affects the phase transition of the BTO [34]. The M-T plot of nanocomposite exhibit the anomaly at the same temperature that indicate the intrinsic magnetoelectric coupling in both the nanocomposites.

Figure 11 displays change in tangent loss with respect to temperature at particular frequency of 10 kHz and it exhibit same behaviour as observed for dielectric constant variation in figure 10. The increasing behaviour of $\tan\delta$ with temperature may be attributed to the thermally activated conduction mechanism [35]. At high temperature the substantial rise of $\tan\delta$ of composites attributed to interfacial polarization at CFO/BTO interface and enhancement of thermally stimulated dielectric relaxation [36].

3.5 Energy storage analysis

Figure 12 displays P-E hysteresis loop at particular frequency 50 Hz for the samples. BTO and nanocomposites exhibit typical ferroelectric behaviour. The value of maximum polarization (P_m), remnant polarization (P_r) and coercivity (E_c) are tabulated in table 3. CFO@BTO sample exhibit highest value of maximum polarization (P_m) at applied electric field of 15 kV/cm which can be ascribed to large number of space polarization occur across the long chain of ordered ferrite/ferroelectric phases.

BTO exhibit small P_m value because ferroelectric behaviour may reduce in nanosized BTO particles due to enhancement in the oxygen vacancies. The P-E loop is used to evaluate energy storage density and storage efficiency of all samples. Energy storage density (W_U) and efficiency (η) can be calculated using the relations [15,37]:

$$W_U = \int_0^{P_{max}} E \cdot dP \tag{6.4}$$

$$\eta = \frac{W_U}{W_U + W_L} \tag{6.5}$$

where E and P represent applied electric field and polarization respectively, W_U and W_L are useful energy storage density and energy loss density respectively. The grey region in P-E loops show the losses and orange region exhibit the recoverable useful energy. CFO@BTO exhibit high efficiency than other samples as depicted in table 3. Therefore these composite samples can be used for storage capacitor devices [38-39].

Table 3
Maximum polarisation (P_m), remnant polarisation (P_r), coercivity (E_c), useful energy storage density (W_U) and energy storage efficiency (η) of samples.

Sample	P_m ($\mu\text{C}/\text{cm}^2$)	P_r ($\mu\text{C}/\text{cm}^2$)	E_c (kV/cm)	W_U (mJ/cm ³)	(%)
BTO	5.96	2.39	11.168	102.31	62.10
CFO@BTO	6.65	2.19	4.54	36.97	64.06
BTO@CFO	7.01	1.66	2.33	19.49	48.01

4 Conclusion

BTO, CFO, their core-shell nanocomposite CFO@BTO and BTO@CFO were synthesized by sol-gel and co-precipitation methods. XRD analysis confirmed that all respective phases are present in bare and nanocomposites sample. HRTEM confirm the core-shell structure and nano size of developed materials.

M-H hysteresis curve showed the typical ferromagnetic behaviour of CFO and core-shell nanocomposites and weak ferromagnetism was observed in BTO sample around $\pm H_c \sim 830$ gauss (excluding diamagnetic part) due to its nanosized effect. CFO@BTO having large value of magnetization and curie temperature than BTO@CFO nanocomposite. Dielectric constant versus temperature curve explained the presence of magneto-electric coupling in composite samples on the basis of anomaly present in curve. First anomaly in temperature range 350-370 K correspond to ferroelectric phase transition in BTO. Another peak in the temperature range 640-680 K was attributed to the transition in dielectric constant close to T_c for CFO phase. The M-T plot of nanocomposite exhibited anomaly in the same temperature range and indicated the intrinsic magneto-electric coupling in both the nanocomposites. Energy storage analysis of the developed samples show that CFO@BTO exhibit energy storage efficiency of 64% which was found higher than other materials present in this work. Thus, all these dielectric, magnetic and ferroelectric properties exhibit that these nanocomposites of ferrite (CFO)/ferroelectric(BTO) phase will be useful for the storage and multistate memory devices

References

1. Eerenstein W, Mathur ND, Scott JF. Multiferroic and magnetoelectric materials. *Nature*. 2006;442:759–65.
2. Spaldin NA, Ramesh R. Advances in magnetoelectric multiferroics. *Nature Mater*. 2019;18:203–12.
3. Raneesh B, Nandakumar K, Saha A, Das D, Soumya H, Philip J, Philip R. Composition-structure-physical property relationship and nonlinear optical properties of multiferroic hexagonal $\text{ErMn}_{1-x}\text{Cr}_x\text{O}_3$ nanoparticles. *RSC Advances*. 2015;5:12480–7.
4. Raneesh B, Soumya H, Philip J, Thomas S, Nandakumar K. Magnetoelectric properties of multiferroic composites $(1-x)\text{ErMnO}_3-x\text{Y}_3\text{Fe}_5\text{O}_{12}$ at room temperature. *J Alloy Comp*. 2014;611:381–5.
5. Wang LG, Zhu CM, Yuan SL, et al. Enhanced room-temperature magnetoelectric effect in $x\text{Bi}_{0.5}\text{Na}_{0.5}\text{TiO}_3-(1-x)\text{NiFe}_2\text{O}_4$ ceramics by magnetic field annealing. *Journal of electroceramic*. 2019;42:113–7.
6. Woldu T, Raneesh B, Sreekanth P, et al. Size dependent nonlinear optical absorption in BaTiO_3 nanoparticles. *Chem Phys Lett*. 2015;625:58–63.
7. Pradhan DK, Choudhary RNP, Nath TK. Magnetoelectric properties of $\text{PbZr}_{0.53}\text{Ti}_{0.47}\text{O}_3-\text{Ni}_{0.65}\text{Zn}_{0.35}\text{Fe}_2\text{O}_4$ multiferroic nanocomposites. *Appl Nanosci*. 2012;2:261–73.
8. Dutta DP, Mandal BP, Naik R, Lawes G, Tyagi AK. Magnetic Ferroelectric and Magnetocapacitive Properties of Sonochemically Synthesized Sc-Doped BiFeO_3 Nanoparticles. *J Phy Chem C*. 2013;117:2382–9.
9. Corral-Flores V, Bueno-Baques D, Ziolo RF. Synthesis and characterization of novel $\text{CoFe}_2\text{O}_4-\text{BaTiO}_3$ multiferroic core-shell-type nanostructures. *Acta mater*. 2010;58:764–9.
10. Chaudhuri RG, Paria S. Core/Shell Nanoparticles: Classes, Properties, Synthesis Mechanisms, Characterization, and Applications. *Chem Rev*. 2012;112:2373–433.

11. Vaz CAF, Hoffman J, et al. Magnetolectric Coupling Effects in Multiferroic Complex Oxide Composite Structures. *Adv Mater.* 2010;22:2900–18.
12. Brown WF, Hornreich RM, Shtrikman S. Upper Bound on the Magnetolectric Susceptibility. *Phys Rev.* 1968;168:574.
13. Etier M, Gao Y, Shvartsman VV, et al. Cobalt Ferrite/Barium Titanate Core/Shell Nanoparticles. *Ferroelectrics.* 2012;438:115–22.
14. Jiang QH, Shen ZJ, Zhou JP, et al. Nan. Magnetolectric composites of nickel ferrite and lead zirconate titanate prepared by spark plasma sintering. *J Eur Ceram Soc.* 2007;27:279–84.
15. Kim DH, Lee HJ, Kim G, et al. Interface electronic structures of BaTiO₃@X nanoparticles (X = γ -Fe₂O₃, Fe₃O₄, α -Fe₂O₃, and Fe) investigated by XAS and XMCD. *Phys Rev B.* 2009;79:033402.
16. Li F, Zeng M, et al. Dielectric characteristics of B-site-modified hexagonal-barium titanate. *J Mater Sci Mater Electron.* 2017;27:2836–40.
17. Puli VS, Pradhan DK, et al. Investigations on structure, ferroelectric, piezoelectric and energy storage properties of barium calcium titanate (BCT) ceramics. *J Alloys Compd.* 2014;584:369–73.
18. Shen Y, Sun J, et al. The enhanced magnetodielectric interaction of (1 – x)BaTiO₃–xCoFe₂O₄ multiferroic composites. *J Mater Chem.* 2014;2:2545–51.
19. Ramana EV, Figueiras F, et al. Observation of magnetolectric coupling and local piezoresponse in modified (Na_{0.5} Bi_{0.5})TiO₃–BaTiO₃–CoFe₂O₄ lead-free composites. *Dalton Trans.* 2014;43:9934–43.
20. Phan TL, Dang NT, Ho TA, et al. First-to-second-order magnetic-phase transformation in La_{0.7}Ca_{0.3}–xBa_xMnO₃ exhibiting large magnetocaloric effect. *J Alloy Comp.* 2016;657:818–34.
21. Qin S, Liu D, et al. UV-Irradiation-Enhanced Ferromagnetism in BaTiO₃. *J Phys Chem Lett.* 2010;1:238.
22. Chaudhuri A, Mandal K. Large magnetolectric properties in CoFe₂O₄:BaTiO₃ core–shell nanocomposites. *J Magn Magn Mater.* 2015;377:441–5.
23. Pal D, Mandal M, Chaudhuri A, Das B, et al. Micelles induced high coercivity in single domain cobalt-ferrite nanoparticles. *J Appl Phys.* 2010;108:124317 (1–5).
24. Zi Z, Sun Y, Zhu X, Yang Z, et al. Synthesis and magnetic properties of CoFe₂O₄ ferrite nanoparticles. *J Mag Mag Mat.* 2009;321:1251–5.
25. Lyubutin S, tarchikov SS, Gervist NE, et al. Canted spin structure and the first order magnetic transition in CoFe₂O₄ nanoparticles coated by amorphous silica. *J Mag Magn Mater.* 2016;415:13–9.
26. Zhou JP, Lv L, Liu Q, Zhang YX, Liu P. Hydrothermal synthesis and properties of NiFe₂O₄@BaTiO₃ composites with well-matched interface. *Sci Techno Adv Mater.* 2012;13:045001 (1–12).
27. Verma KC, Singh M, Kotnala RK, Goyal N. Magnetic field control of polarization/capacitance/voltage/resistance through lattice strain in BaTiO₃-CoFe₂O₄ multiferroic nanocomposite. *J Mag Magn Mater.* 2019;469:483–93.

28. Sirdeshmukh L, Kumar KK, Laxman SB. Dielectric properties and electrical conduction in yttrium iron garnet (YIG). *Bull Mater Sci*. 1998;21:219–26.
29. Kumari N, Kumar V, Singh SK. Synthesis, structural and dielectric properties of Cr³⁺ substituted Fe₃O₄ nanoparticles. *Ceram Int*. 2014;40:12199–205.
30. Janal PK, Sarkar S, Chaudhuri BK. Maxwell–Wagner polarization mechanism in potassium and titanium doped nickel oxide showing giant dielectric permittivity. *J Phys D Appl Phys*. 2007;40:556–60.
31. Kumar A, Yadav KL. Synthesis and characterization of MnFe₂O₄–BiFeO₃ multiferroic composites. *Phy B*. 2011;406:1763–6.
32. Koops CG. On the Dispersion of Resistivity and Dielectric Constant of Some Semiconductors at Audiofrequencies. *Phys Rev*. 1951;83:121.
33. Wu YC, Fan YZ, Liu NT, et al (2019) Enhanced energy storage properties in sodium bismuth titanate-based ceramics for dielectric capacitor applications. *J Mater Chem C* 2019, 7: 6222–6230.
34. Patil DR, Chougale SS, et al. Electrical properties of xNiFe₂O₄+(1 – x)Ba_{0.7}Sr_{0.3}TiO₃ composites. *J Alloy Compd*. 2008;452:414–8.
35. Zhao Z, Buscaglia V, Viviani M, et al. Grain-size effects on the ferroelectric behavior of dense nanocrystalline BaTiO₃ ceramics. *Phys Rev B*. 2004;70:024107 (1–8).
36. Fawzi AS, Sheikh AD, et al. Composition dependent electrical, dielectric, magnetic and magnetoelectric properties of (x)Co_{0.5}Zn_{0.5}Fe₂O₄ + (1 – x)PLZT composites. *J Alloy Compd*. 2010;493:601–8.
37. Basu S, Babu R, Choudhary KR RNP. Studies on the piezoelectric and magnetostrictive phase distribution in lead zirconate titanate–cobalt iron oxide composites. *Mater Chem Phys*. 2010;132:570–80.
38. Puli VS, Pradhan DK, et al. Investigations on structure, ferroelectric, piezoelectric and energy storage properties of barium calcium titanate (BCT) ceramics. *J Alloys Compd*. 2014;584:369–73.
39. Shankar S, Kumar M, Tuli V, Thakur OP, Jayasimhadri M. Energy storage and magnetoelectric coupling in ferroelectric-ferrite composites. *J Mater Sci Mater Electron*. 2018;29:352–18357.
40. Li Q, Zhang WM, Wang C, et al. Enhanced energy-storage performance of (1-x) (0.72Bi_{0.5}Na_{0.5}TiO₃-0.28Bi_{0.2}Sr_{0.7-0.1}TiO₃)- (x)La ceramics. *J Alloys Compd*. 2019;775:116–23.

Figures

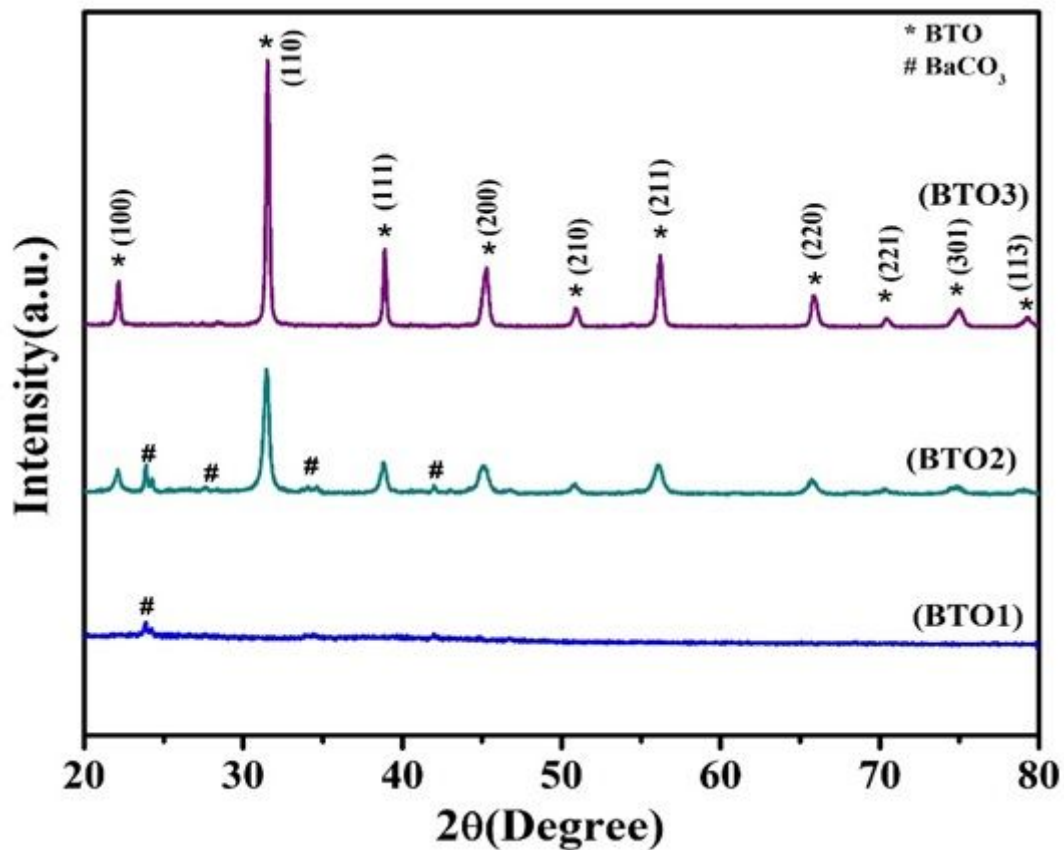


Figure 1

XRD pattern of BTO nanoparticles at different annealing temperature represented by BTO1 (without annealing), BTO2 (600 °C) and BTO3 (800 °C).

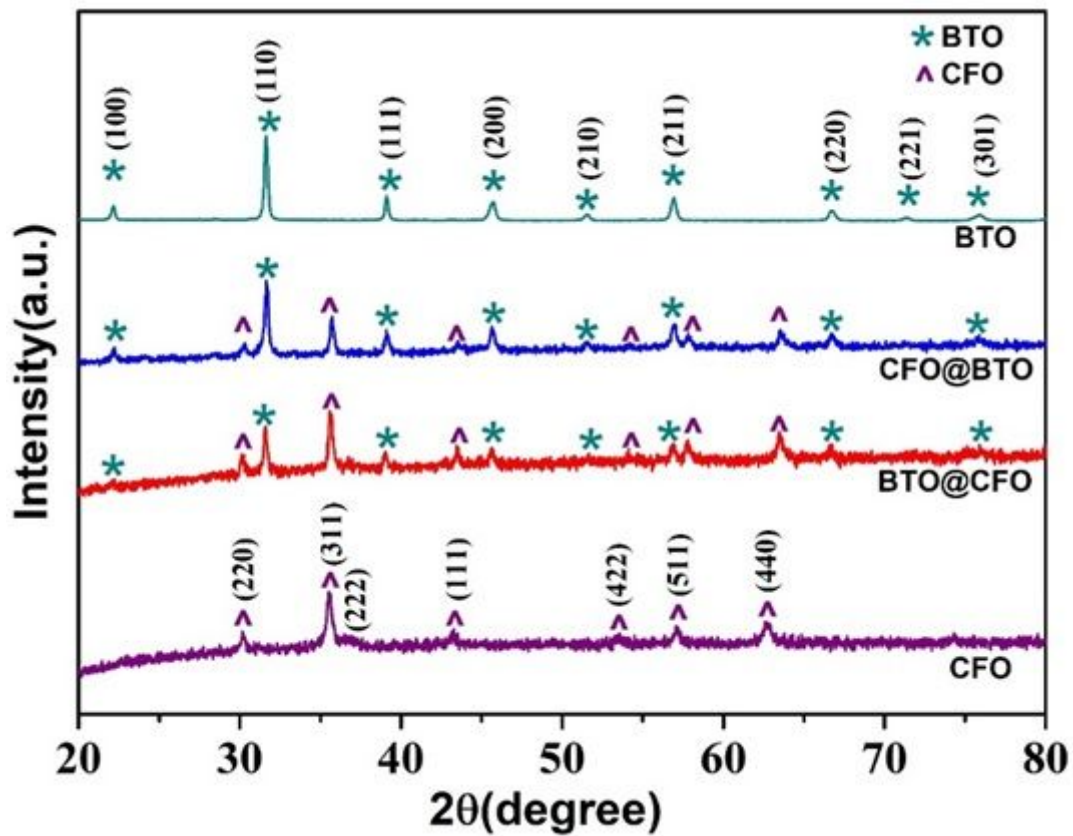


Figure 2

XRD Pattern of CFO, BTO @CFO , CFO @BTO and BTO. '*' and '^' represent BTO and CFO phase respectively.

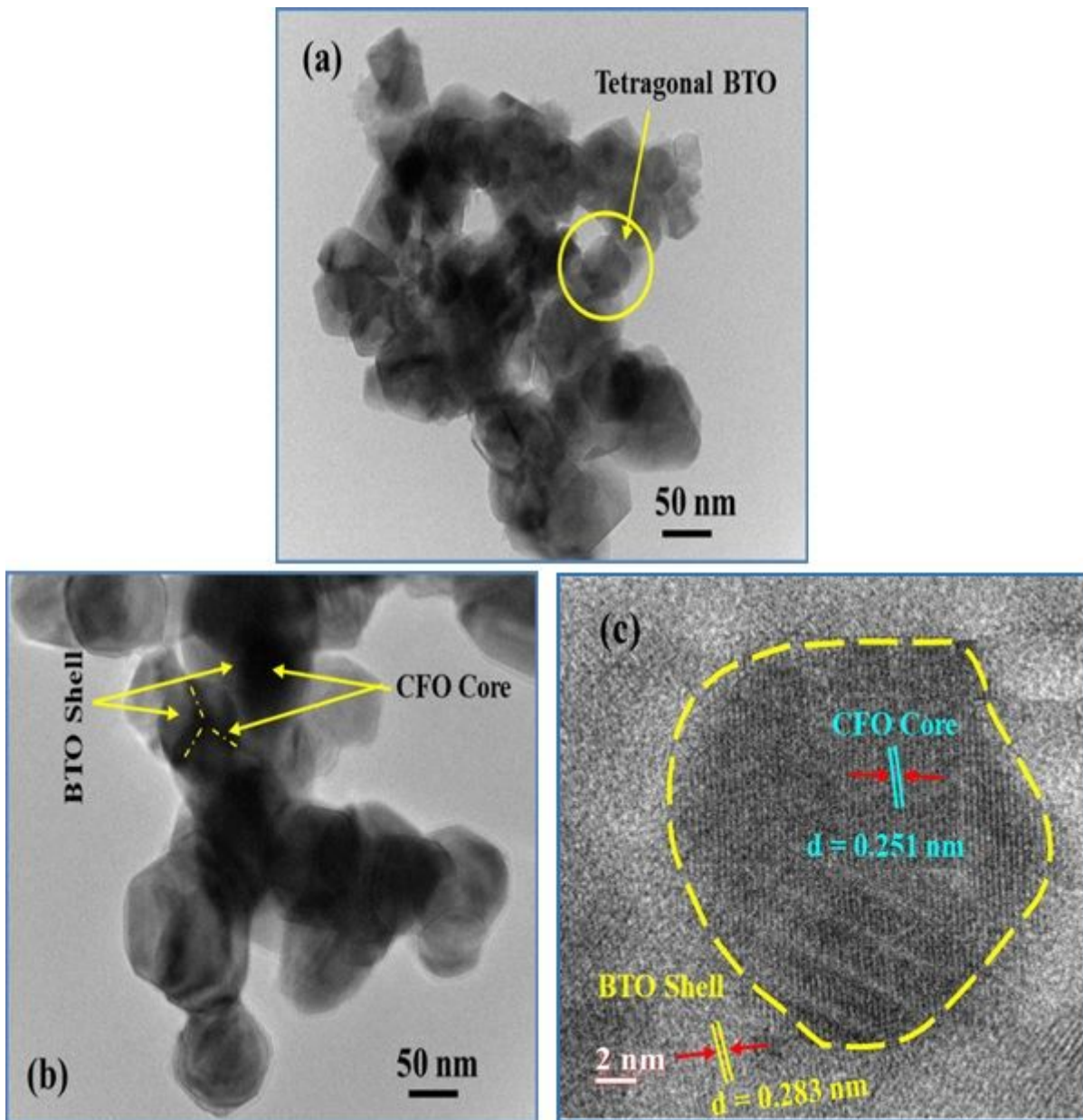


Figure 3

HRTEM micrograph of (a) BTO (b) CFO@BTO (c) magnified view of CFO@BTO represent d spacing of individual phases.

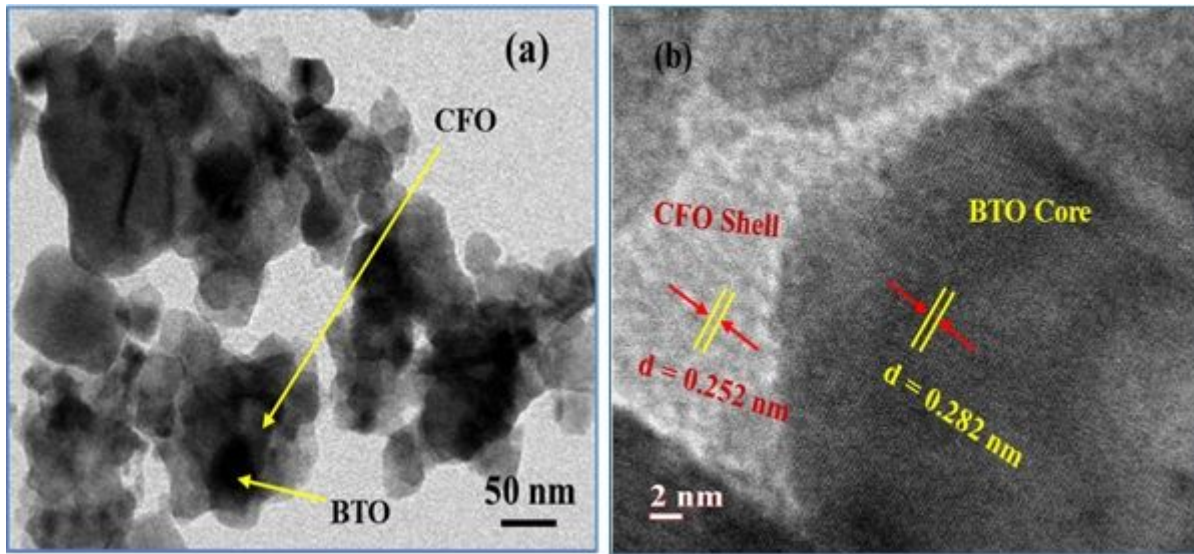


Figure 4

HRTEM micrograph of (a) BTO@CFO (b)magnified view of BFO@CFO represent d spacing of individual phases.

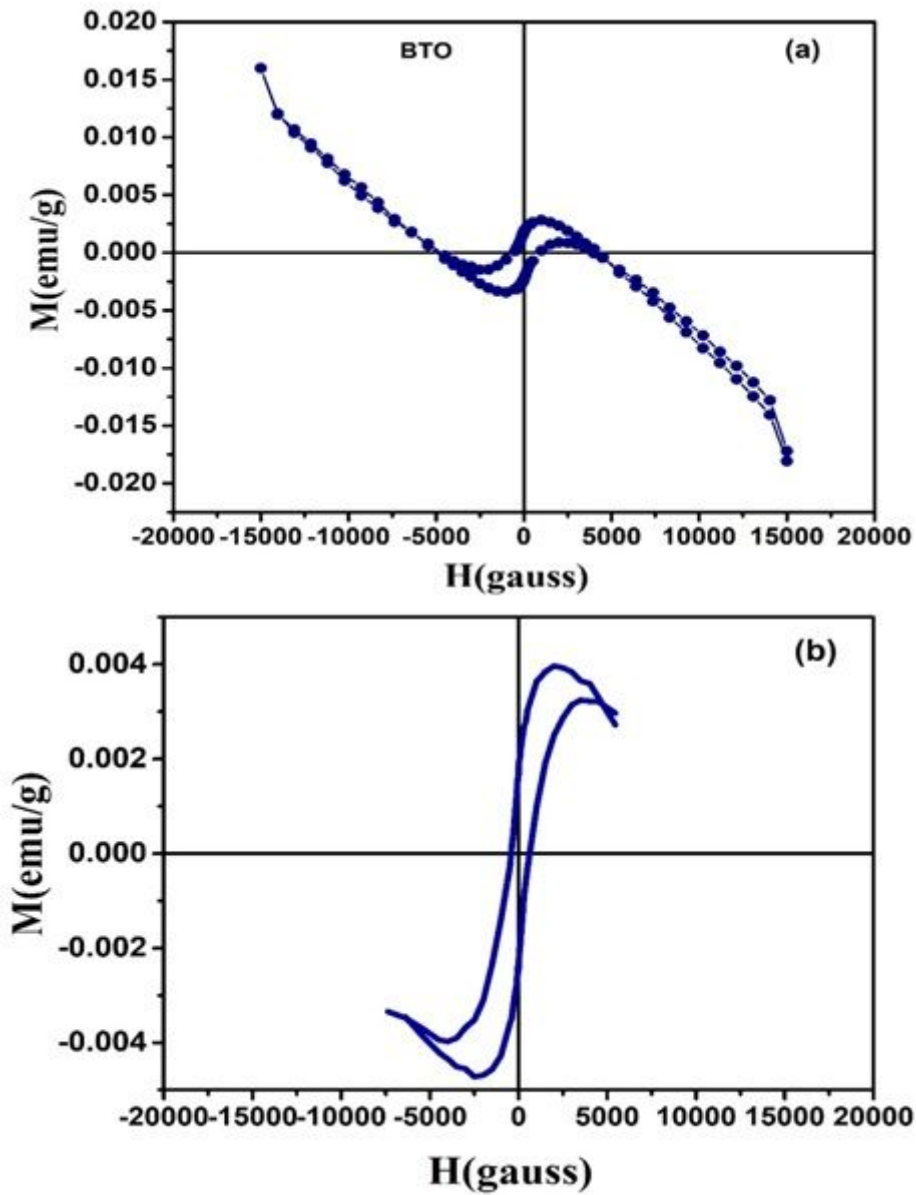


Figure 5

(a) M-H plot for BTO nanoparticles and (b) M-H curve obtained after excluding the diamagnetic contribution from M-H plot of BTO.

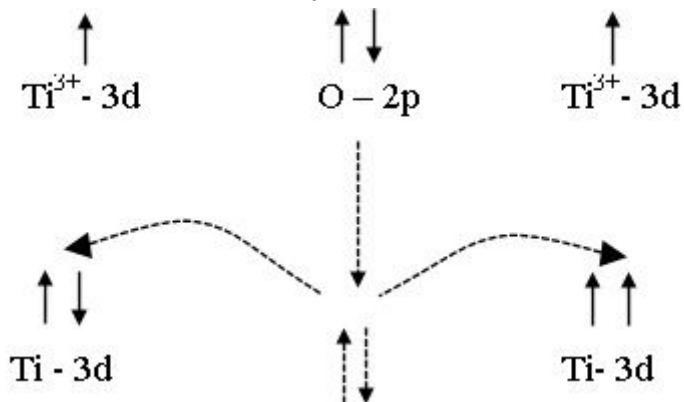


Figure 6

Mechanism of ferromagnetic exchange interaction in BTO nanoparticles

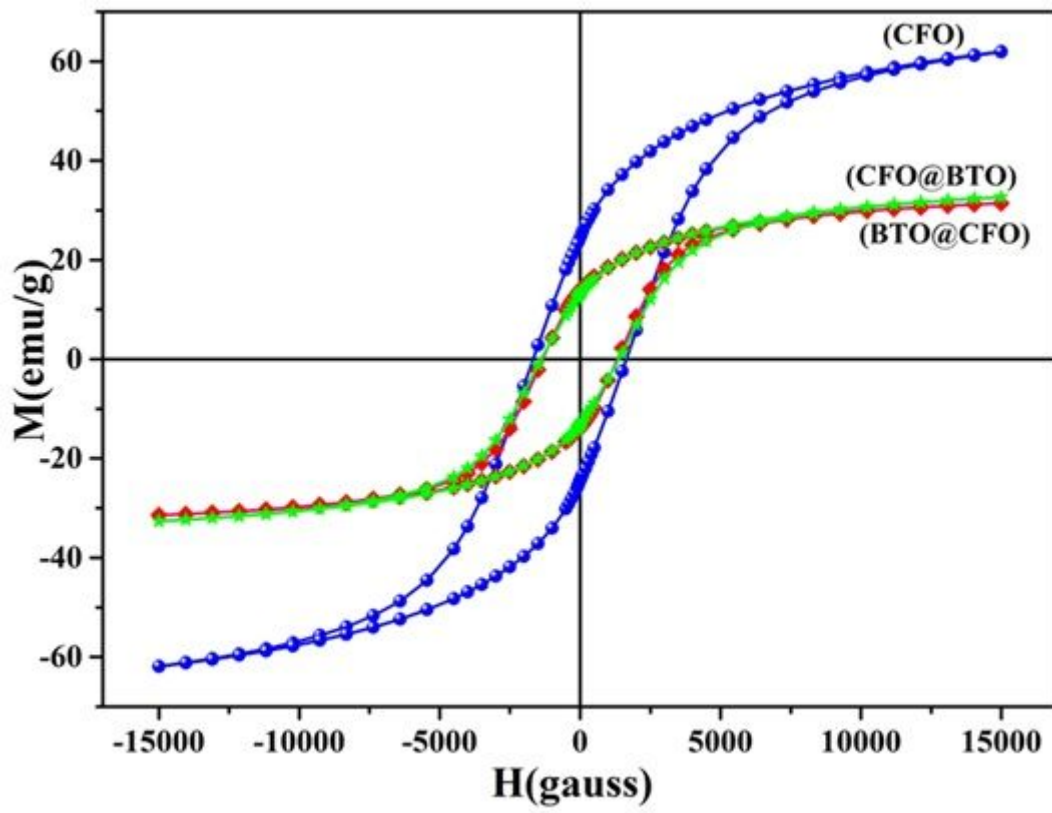


Figure 7

M-H loop of CFO, CFO@BTO and BTO@CFO nanoparticles.

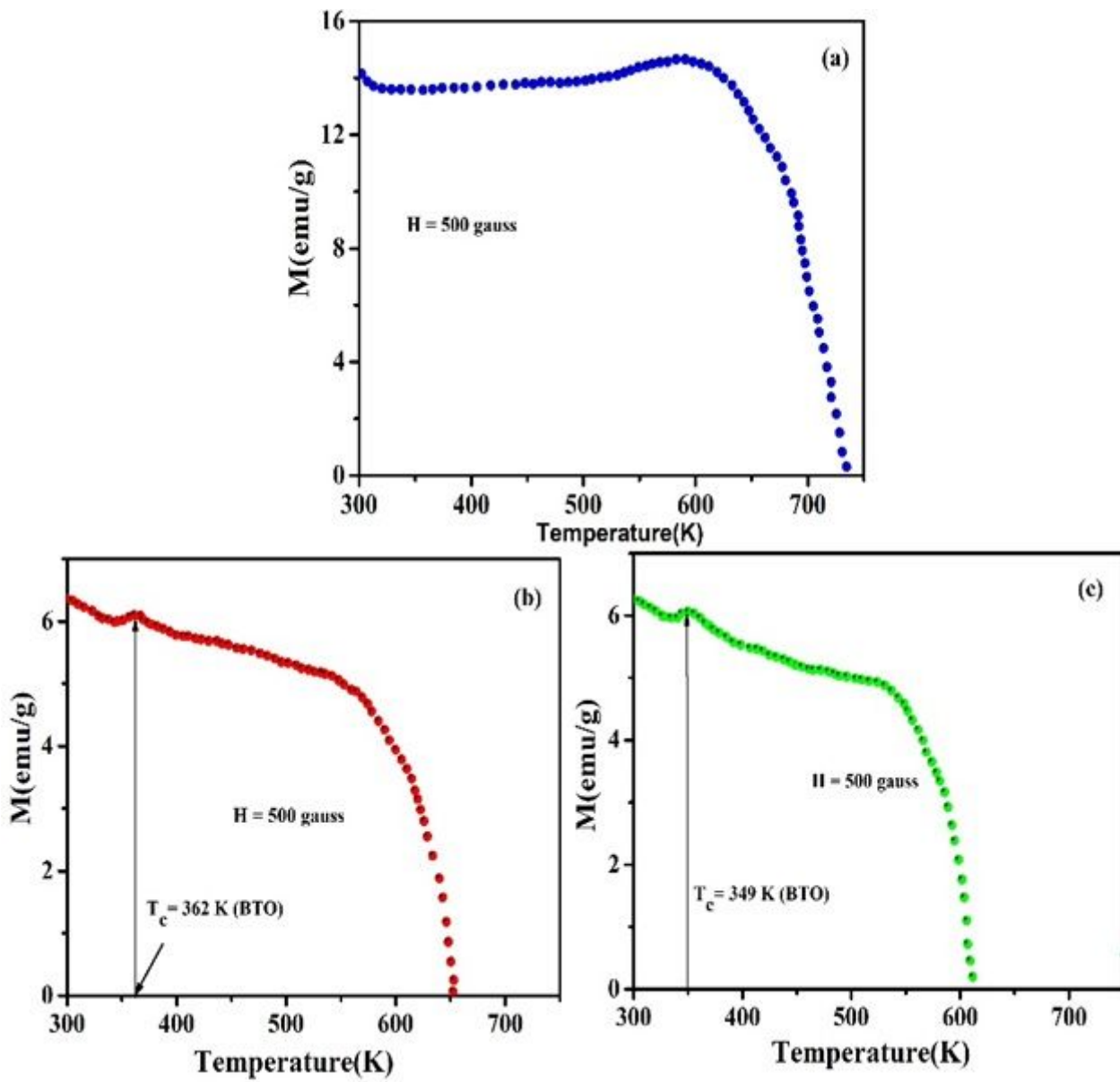


Figure 8

Magnetisation versus temperature (M-T) plot at applied magnetic field of 500 gauss of (a) CFO, (b) CFO@BTO, and (c) BTO@CFO nanoparticles

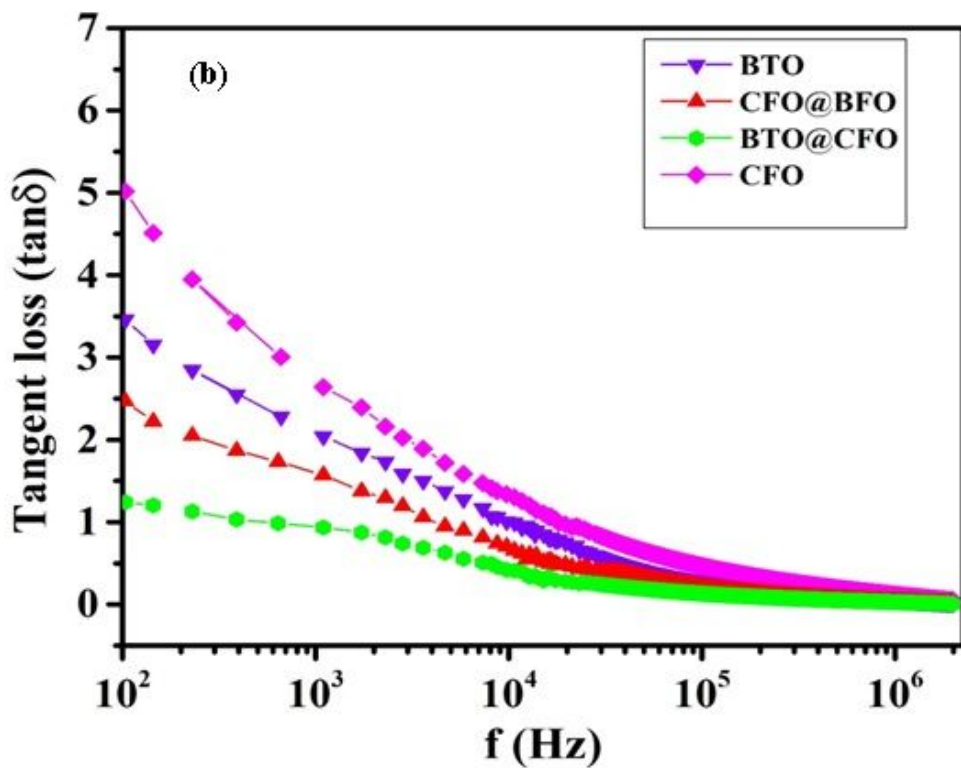
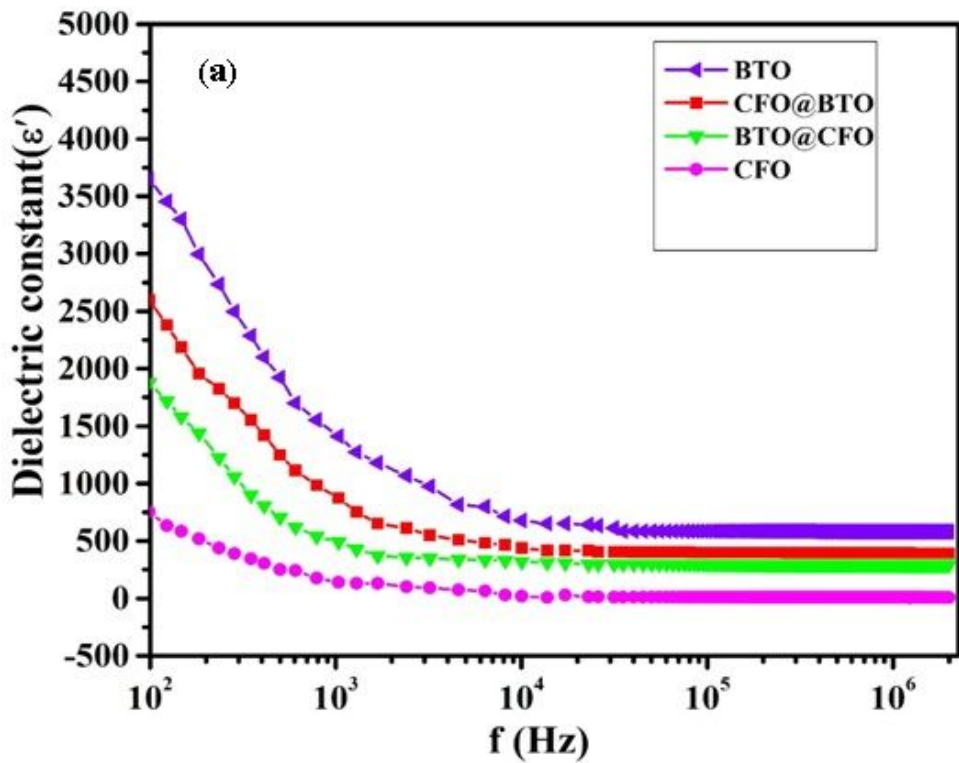


Figure 9

Frequency dependent behaviour with (a) dielectric constant (b) tangent loss of BTO, CFO, CFO@BTO and BTO@CFO nanoparticles at room temperature.

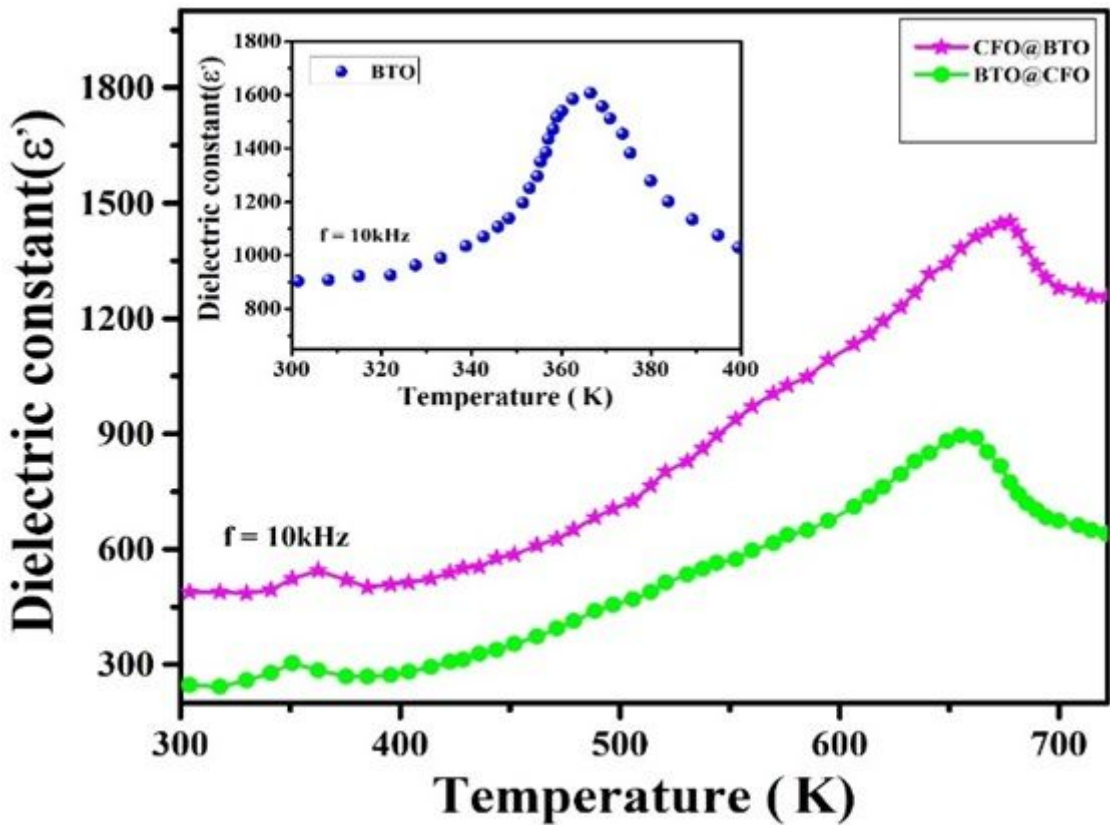


Figure 10

Temperature dependent dielectric constant of BTO (in inset), CFO@BTO and BTO@CFO nanoparticles at fixed frequency of 10 kHz

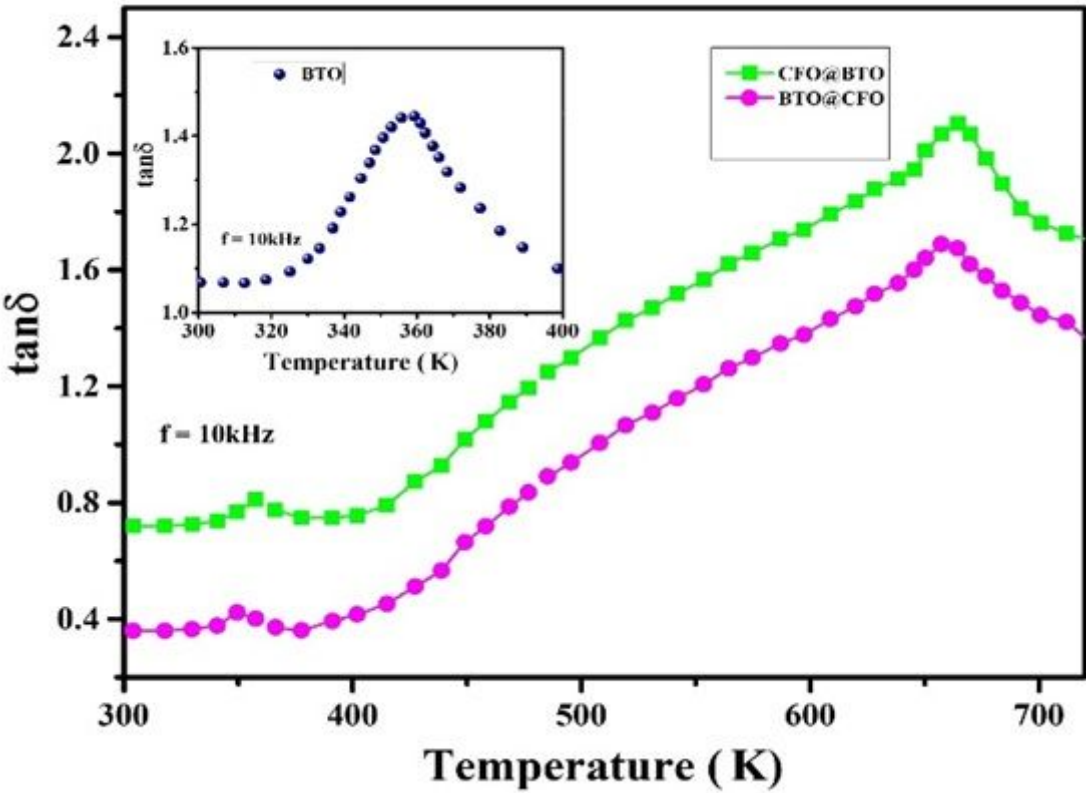


Figure 11

Temperature dependent $\tan\delta$ (tangent loss) of BTO (in inset), CFO@BTO and BTO@CFO nanoparticles at fixed frequency of 10 kHz.

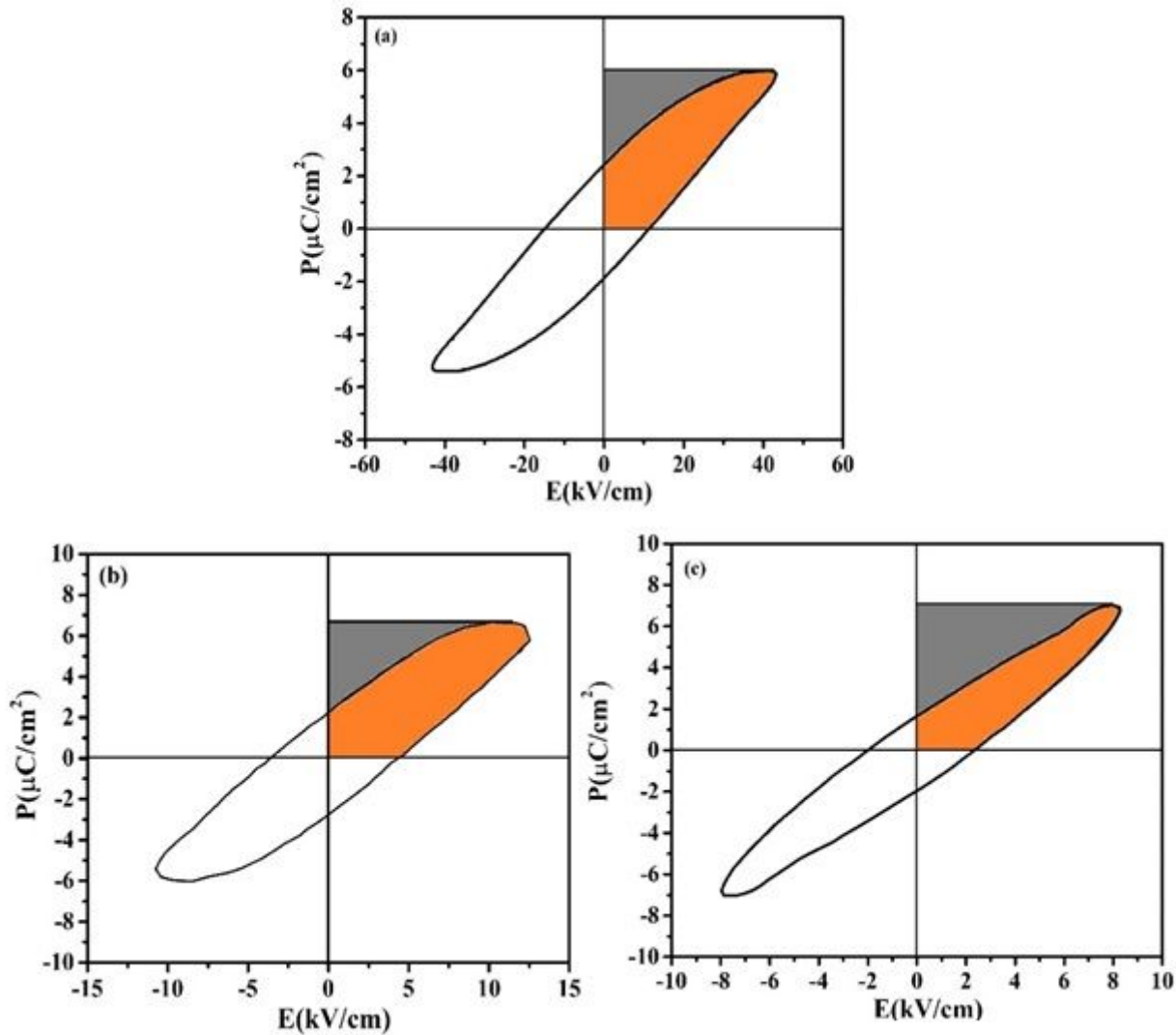


Figure 12

P-E loop behavior of BTO, CFO@BTO and BTO@CFO nanoparticles at room temperature.